Ice crystal habits from cloud chamber studies obtained by in-line holographic microscopy related to depolarization measurements

Peter Amsler,[1,*] Olaf Stetzer,[1] Martin Schnaiter,[2] Evelyn Hesse,[3] Stefan Benz,[2] Ottmar Moehler,[2] and Ulrike Lohmann[1]

[1] *ETH Zurich Institute for Atmospheric and Climate Science, Universitaetstrasse 16, 8092 Zurich, Switzerland.*

[2] *Institute of Meteorology and Climate Research, Forschungszentrum Karlsruhe, Karlsruhe, Germany*

[3] *University of Hertfordshire, Centre for Atmospheric and Instrumentation, Research, Hatfield, Hertfordshire AL10 9AB, UK*

[*] *Corresponding author: peter.amsler@env.ethz.ch*

Hydrometeor habits have been investigated at the AIDA chamber with a newly developed in-line holographic microscope HOLIMO (HOLographic Imager for Microscopic Objects). Sizes and habits of ice crystals and droplets in a mixed-phase cloud experiment were related to relative humidity with respect to ice (RH_{ice}), temperature (T) and experiment time. This experiment was initiated with supercooled water drops. As a result, ice crystals within a maximum particle diameter size range of 2 μm to 118 μm (average size of 19 μm) have been detected and 63% of them revealed regular habits. The observed particle habits matched those predicted for a given RH_{ice} and T. Two different growth modes emerged from this cloud. The first one appeared during water injection and revealed mainly optical particle sizes in the range of 5 to 250 μm. The second mode grew to sizes of 5 to 63 μm, just after the particles of the first one fell out. It was found that an increasing aspect ratio χ of maximum length over thickness from 2 to 20 as obtained by HOLIMO corresponds to a decreasing linear depolarization ratio from 0.1 to 0.04 as independently obtained by depolarization measurements.

OCIS codes: 090.1995, 010.2940.

1. Introduction

The ability of aerosols to act as ice nuclei is a subject of intense investigations. Much has been learned about ice nucleation, its importance for microphysical processes, precipitation formation and optical properties of clouds [1–5]. Nevertheless, a comprehensive theory for heterogeneous ice nucleation is still lacking [6]. Therefore, it is necessary to obtain a better knowledge about the efficiency of aerosols to nucleate ice. Once nucleated the ice crystal growth will depend on relative humidity and temperature [7]. Different environmental conditions during ice nucleation lead to different ice crystal habits. Those habits have different scattering properties and depolarize light differently [5, 8]. Consequently, it is important to know the aerosol type, the conditions during ice formation and the ice crystals habit and orientation. This issue can be addressed in laboratory experiments for instance when combining ice nucleation chambers with holographic instruments.

Holographic probes of different kinds are widely used. Kreuzer et al. (2001) made holograms obtained by an electron point source in order to investigate polymer structures [9]. Trolinger (1975) investigated jets and sprays coming from a nozzle [10]. Apart from that, also living organisms were widely studied with holograms obtained by a laser point source of light [9]. Even their 3D distribution and motion were investigated [11]. Also in the field of Atmospheric and Climate Science holographic probes are used. For instance, Brown (1989) and Fugal et al. (2004) used a holographic

probe for air borne measurements of hydrometeors [12, 13]. Others like Vossing et al. (1998) or Raupach et al. (2006) investigated atmospheric hydrometeors from the ground [14, 15].

In this paper the HOLIMO (HOLographic Instrument for Microscopic Objects) detector and results obtained with this device will be presented in sections 2 and 4 respectively. This paper focusses on the relation of optical properties of ice crystals and their habits in an existing cloud. Section 3 describes the AIDA cloud chamber where the above mentioned experiments have been carried out in November 2007. A holographic microscope was used because the principle of this technique allows for producing 2D images with high and 3D shapes with reduced resolution of ice crystals throughout the whole observing volume V_{obs} (see appendix for the description of symbols). That means that depth of focus, as is crucial for optical microscopy, is not important for this system. This increases the number of particles that can be detected and analyzed automatically during a measurement provided that the information is recorded digitally, i.e. with a camera. It has been shown that holographic probes can resolve objects down to a size of 1 μm [9].

2. The holographic microscope HOLIMO

HOLIMO is a Point Source Digital In-line Holographic Microscope constructed in our research group. It consists of a laser, an optical fiber, a camera, two windows and a small chamber confining the particle flow. With this setup one is able to determine

size, position, orientation and shape of objects coming from a sample inlet. Figure 1 shows a sketch of the working principle of this instrument and an example image of interference fringes as it can be observed on a screen. A laser pulse with a pulse length of 1 ns, a pulse energy of 0.32 μJ and a wavelength of 532 nm is coupled into a single mode fiber of 3.5 μm core diameter. The fiber end acts as a point source (PS) of light. Eventually, the coherent light is scattered off from an object inside the light cone, defined by the divergence of the PS. This object is sucked through a sample flow tube with a diameter of 4 mm. The resulting coherent interference pattern is then recorded with a digital camera sensor. The camera (SVS4021 12BIT-S/VISTEK) and the laser (FDDS532-Q2/CryLas) are sealed off from the sample flow with two windows. The single mode fiber ensures that the laser pulse is a single mode single frequency pulse. As such the spectral width of the laser will be proportional to its coherence length $c(\pi\nu)^{-1}$ which is the relative travelling distance between the undisturbed reference wave and the scattered wave amplitude. Hence, it is a spatial and a temporal coherence length. The laser used in HOLIMO has a coherence length of 5 cm. The divergence of the single mode fiber and the setup of HOLIMO defines a light cone with a V_{obs} of about 8.3 mm^3 (hatched area of figure 1) appropriate for in-situ measurements of cloud particles. The exact volume is hard to define because, due to the Gaussian intensity distribution of the PS, there is the possibility that objects outside the light cone can scatter light back towards the camera.

2.1. Theory of operation

The distance from the PS to the camera divided by the distance from the PS to the object defines the geometrical magnification m_1. With a PS to camera distance of L=132.5 mm and a PS to object distance l between 7.2 and 11.7 mm, m_1 is roughly between 11 and 18. This is true for point objects and spherical wave fronts in one medium. Otherwise, the magnification is changed as the wave front changes either in shape or divergence. The overall magnification is then $M = m_0 m_1$. The magnification m_0 depends on the wavelength. For one medium m_0 is given as the product $\lambda_{eff}^{-1}\lambda = n_1\lambda^{-1}\lambda = n_1$, where n_1 is the refractive index of and λ_{eff} the wavelength inside the window material. In our application

$$\begin{aligned} \lambda_{eff} &= \lambda m_0^{-1} = \lambda \frac{s_1 + s_2 + s_3 + s_4 + s_5}{n_1 s_1 + n_2 s_2 + n_3 s_3 + n_4 s_4 + n_5 s_5} \\ &= 532 \text{ nm} \cdot \frac{132.5 \text{ mm}}{140.8 \text{ mm}} = 501 \text{ nm}, \end{aligned} \tag{1}$$

where s_1, s_3, s_5 are the travelling distances of the laser beam in air and s_2 and s_4 are the travelling distances of the laser beam inside the windows with the appropriate refractive index $n_1 = n_3 = n_5 = 1$ and $n_2 = n_4 = 1.517$ [16]. The first window has a thickness of 6 mm and the second of 10 mm. This wavelength dependence becomes particularly important when a particle sits on a window. For a particle inside V_{obs} on the window closest to the PS $m_0 > 1$ because light eventually passes directly from the glass to the particle. Thus the particle appears to be 1.3 mm closer to the PS than it

is and its size will be overestimated by 22%. On the contrary, the size of particles will be underestimated by 22% if they sit on the window closest to the camera inside V_{obs}. This wavelength dependence results in a sizing error that needs to be corrected for. A calibration with 20.2 μm PSL spheres yielded an average sizing error of HOLIMO of 15% for particles inside V_{obs} not touching any window.

The interference pattern is treated with the Kirchhoff-Helmholtz transformation in order to obtain a real image of the object [17]. This is appropriate because the lower size resolution limit of HOLIMO is around 5 μm resulting in a Mie size parameter (see subsection "resolution considerations") much larger than 1. Therefore, we are in the Kirchhoff regime. As a consequence, the object needs to be at far field distances from both the point source of light and the camera. The far field condition is $x_{crit} \geq (2a)^2\lambda^{-1}$. This takes the maximum diameter $2a$ of the object and the wavelength λ of the PS into account [13]. For a spherical object with a diameter of 5 μm and with a wavelength of 532 nm this condition would be met after 47 μm. With HOLIMO a maximum amount of far field distances $N = \lambda l M(2a)^{-2} = 2809$ would be possible between the PS and 5 μm sized particles in the current setup. Such high values, owing to the large overall magnification M, are ideal for intensity reasons. The overall intensity drops with increasing N values (see below) but the image to background intensity ratio increases [18]. Equation (2) shows the Kirchhoff-Helmholtz transformation and how it is applied numerically to HOLIMO.

$$
\begin{aligned}
K(\vec{r}) &= \int_A d^2\vec{\xi}\tilde{I} exp\left(\frac{2\pi i \vec{\xi}\vec{r}}{\lambda\xi}\right) \\
K(k,p;l) &= \sum_{h=-n/2}^{n/2}\sum_{j=-n/2}^{n/2} \tilde{I}(h,j;L) exp\left(\frac{2\pi i}{\lambda}\left(\frac{\tilde{k}\tilde{h}+\tilde{p}\tilde{j}+lL}{\sqrt{\tilde{h}^2+\tilde{j}^2+L^2}}\right)\right)
\end{aligned}
\tag{2}
$$

K is one point of the reconstructed plane calculated at the point r inside V_{obs} and related to all the points ξ on the camera sensor by the light intensity $\tilde{I}$ at these points at a fixed longitudinal distance L. Since the sensor of a camera has a finite amount of pixels equation (2) can be written as a double sum over n integers h and j. The expressions with tilde in this equation represent distances in pixel size Δ_X and Δ_Y on the camera sensor and $\Delta_x = \Delta_X/M$ and $\Delta_y = \Delta_Y/M$ on the reconstructed image plane with respect to the center. For instance, $\tilde{p} = p\Delta_x$. K then is one point (k,p) of the reconstructed plane at a fixed longitudinal position l inside V_{obs} related to all points (h,j) on the camera sensor by the light intensity $\tilde{I}$ at their positions at a fixed longitudinal distance L.

Note that the integral expression of equation (2) does not determine the field of view of the reconstruction. The extent of the reconstructed images increases towards the camera when scaling the reconstructed distance and size. Consequently, the pixel sizes Δ_x and Δ_y of the reconstruction plane get larger with increasing distance from the PS (see figure 2).

2.2. Resolution considerations

The resolution of a coherent imaging system with respect to the numerical aperture NA is one way to determine the resolution of HOLIMO. The minimum size of the object is given as $d_{lat} = \lambda(NA)^{-1}$ (lateral dimension) and $d_{long} = \lambda(NA)^{-2}$ (longitudinal dimension) [19]. There are also calculations that take the object position within V_{obs} into account [16]. The resolution of a holographic instrument can be calculated very accurately but this does not necessarily lead to a more precise resolution limit. There are lots of other factors that influence the resolution of the system. For instance, there is the resolution of the camera sensor i.e. the amount of pixels ($N_{pix} = n \cdot n$). HOLIMO has a maximum $N_{pix} = 2048 \cdot 2048 = 4'194'304$ with $\Delta_X = \Delta_Y = 7.4$ μm. If this resolution is too small the interference pattern will be undersampled. Then the image will contain a lot of noise which, in the worst case, could hinder the detection of particles [20]. This sampling criteria is dependent on m_1. If m_1 is small then N_{pix} needs to be large. By far the most important point for the resolution consideration is that the camera needs to record as many interference fringes as possible. This leads to the counter intuitive statement that m_1 needs to be smaller rather than larger because edge smearing will then be reduced. Robinson (1970) calculated the relative edge smear w for a long wire of thickness $2a$ as a function of the number of side lobes m of the interference pattern [21]. Although derived for this special case he found the result $w(2a)^{-1} = (2m)^{-1}$ being valid for general cases as a worst case scenario.

More quantitatively, particles with circular cross section will have a fringe spacing $\Delta r = 2a(1+m)^{-1}$ according to Cartwright et al. (1980) [22]. The maximal recordable radial distance is given by $r_{max} = (1+m)z\lambda M(2a)^{-1}$, with z being the distance between object and camera. Via conversion, the maximal recordable amount of interference fringes $m = 2ar_{max}(\lambda z M)^{-1} - 1$ can be obtained, with $r_{max} = 2048 \cdot 7.4$ μm=15 mm being the maximum extension on the camera chip. This results in 9 fringes for a particle with a diameter of 5 μm, z =14 mm and $M = 1$. The relative edge smear would then be 11%. Using spherical objects for resolution considerations is the worst case scenario because they reveal the worst resolution among all possible shapes. This is due to the curvature of their boundary. Therefore, they are more susceptible to noise as compared to a non-spherical object of the same size [22]. In general it is agreed that $m = 3$ leads to a sharp enough image of the object [22]. Additionally, spatial frequencies for coherent imaging $\nu = 2\pi r(\lambda z M)^{-1} = 8\pi(2a)^{-1}$ become independent of everything but the object size if $r = r_{max}$ [23]. Because the single mode single frequency laser pulse has a Gaussian intensity distribution, the fringe visibility V for opaque objects varies as MN^{-1} [20]. This is larger than for a uniform intensity distribution. It therefore makes sense, due to the complexity of the subject, to account only for λ and NA for resolution discussions. The numerical aperture of the used mono mode fibre in the far field is given by $NA_{eff} = 2\lambda(\pi MFD)^{-1}$ where MFD, the mode field diameter, equals 4.2 μm. This results in $NA_{eff} = 0.08$ which is equivalent to an aperture angle of 4.6°. An optical microscope with such an

aperture angle would have a resolution limit of $d = \lambda(n \sin \alpha)^{-1} = \lambda(NA)^{-1}$ =6.6 μm [24]. It is the same as the lateral resolution of a coherent imaging system with respect to NA. As a consequence, for $M > 1.15$, the pixel size of the focal plane would be smaller than the resolution limit of diffraction for a pixel size of 7.4 μm of the recording plane. In other words, optical microscopes start to diffract objects of a size smaller than the Abbe limit and therefore, overestimate the size of the object. In general, holographic microscopes, having no fixed focal plane, can reproduce object sizes more reliably.

In a first step, HOLIMO was optimized with respect to the maximum recordable area of the light cone which is defined as the area where the light intensity is higher or equal to the maximum intensity $I_0 \exp(-1)$. This means that the CCD chip (a square) is inscribed into the light cone from the divergent PS (see figure 1). Whether the area of the camera sensor suffices for a clearly resolvable reconstruction of the object is hard to answer because it depends above all on the comparison of object sizes with the wavelength of the instrument. Mie theory provides an analytical expression for this comparison with its size parameter ($\pi 2a\lambda^{-1}$). If this size parameter is at least ten times larger than 1 then there will be only forward scattered light within an angle of 3° [13]. With this small divergence angle it is guaranteed that sufficient interference fringes for reconstruction will be recorded with HOLIMO. For instance for a wavelength of 532 nm and a spherical object of 5 μm diameter this size parameter is 29.5.

2.3. Particle hitting rate

HOLIMO has a V_{obs} of 8.3 mm^3 with respect to the Gaussian intensity distribution of the PS. The maximum speed of the camera is 4 frames per second. This means that HOLIMO is able to record $4V_{obs}$ per second. Therefore, the particle hitting rate is $c4V_{obs}\mathrm{s}^{-1}$. This formula depends on the concentration c but it is independent of the particle flow. HOLIMO sees about 1 particle per 30 s if $c = 1$ cm^{-3}. Nonetheless, it is important to deal with motion blurring if the velocity of the particle flow is too high. A rule of thumb is to allow a spherical particle to move 10% of its size in the worst case. The laser used has a pulse length of 1 ns. Therefore, for a flow of 10 l min^{-1}, the motion blur would be 53 nm which is less than 10% for a spherical object of 1 μm. Hence there is an upper limit to the flow concerning motion blur.

There is also a limit to the flow concerning laminar or turbulent flow regimes. For a tube Reynolds number < 2300 the flow will always be laminar. Depending on the setup of the experiment, the flow might still be laminar even above a tube Reynolds number of 2300.

2.4. Data processing

In order to find particles at their correct position inside V_{obs}, one has to find a scanning algorithm that eliminates unwanted/unfocused image planes. From now on this is being referred to as plane stacking. Trolinger (1975) found that coherent imaging has a big advantage over conventional imaging when it comes to the question of

auto focussing [10]. He found a way that was easy to apply noting that the average intensity increases towards the focal plane. Thus the particle can be found inside V_{obs} by searching for the reconstructed image with maximum average intensity. This agrees with our findings. After the brightest image is found, the maximum and the minimum of the average intensities of all reconstruction planes yield the thresholds for the upper and lower limit for a segmentation resulting in a binary representation of the image. Thus the particle can be identified. Center of mass, outer and inner circumference, area and total area $\tilde{A}$ inside the outer circumference of the object are then determined from the binary picture. The center of mass can help to omit pixels that are wrongly attributed to the object due to the chosen threshold of segmentation. This means that there is noise. If the noise is far away from the object then everything outside the radius containing the object will be attributed to the background signal. Finally, a boundary box is determined and a classification of the images of the particles can be done.

Earlier works classified images of ice crystals in a great variety of classes and subclasses by eye [25]. Korolev et al. (2000) classified their data automatically into the 4 major habits for cloud particles, namely circular, dendrites/aggregates, columns/needles and irregulars [26]. They also found that classifying data in this way can be done most unambiguously. For HOLIMO only three classes were used, namely droplikes (corresponding to circular in [26]), regulars and irregulars. Later discrimination of regulars into hexagonal and non-hexagonal shapes (including needles and

dendrites) and irregulars into pristine shapes with imperfections and aggregates where the individual pristine shapes are still visible was done by eye.

Figure 3 shows the automated process in a flow chart illustrated with an example. We decided to take the maximum dimensions in the vertical (D_w) and horizontal (D_{max}) directions since the expected particle habits at the given atmospheric conditions for the experiment discussed here are plate-like crystals. The emerging plates were large enough to orientate themselves horizontally inside the sample tube before arriving at the sample volume. Additionally, the apparent area $\overline{A}$ of the object is determined. In this way, the aspect ratio $\alpha = D_w D_{max}^{-1}$, the roundness $\beta = 4\overline{A}(\pi D_{max}^2)^{-1}$ and the equivalent sphere diameter $d_{equiv} = 2(\overline{A}\pi^{-1})^{1/2}$ (used for comparison of round and regular shapes with $\alpha \approx 1$), allow for classification into the three classes mentioned above. Figure 4 shows α and β for different simple examples calculated analytically. Hydrometeor habits can never be classified according to those simple shapes since α and β alone do not provide sufficient information. They depend on the reconstruction process and its ability to find the right focal plane. The analysis of several experiments leads to a rough estimation of the range of α and β but the outcome needs to be controlled by eye.

Furthermore, the reconstruction plane separation Δl, the threshold and the particles that are halfway over or fully outside of the Gaussian aperture can cause problems for the automated classification process since the particles can be out-of focus, the background noise can be large or the particles true habit might not be recognized.

Additionally, they can be too small or may occlude one another and hence will be wrongly associated with their sizes. Thus, the habits may be attributed to a wrong class. As a consequence, Δl needs to be decreased in order to obtain an in-focus reconstruction and to reduce the noise of the binarized image. This however leads to a larger number of reconstruction planes to be stacked inside V_{obs} and therefore to an increased computing time. Shapes of particles smaller than 10 μm can not be distinguished if m_1 and/or m are too small.

3. AIDA facility

The HOLIMO detector described in section 2 has been applied in the ice nucleation campaign IN11 which has been conducted in November 2007 at the cloud chamber AIDA of Forschungszentrum Karlsruhe [27]. These experiments aim to improve our knowledge of the ice nucleation and growth processes in atmospheric mixed-phase and ice clouds. Such clouds can be simulated in AIDA by controlled expansion cooling experiments which mimic the adiabatic expansion cooling of rising air parcels in the atmosphere. Experiments can be performed over a broad temperature range down to 183 K. The huge chamber volume of 84 m^3 thereby enables cloud maintenance times of up to 30 minutes. During IN11, several specific ice cloud characterization experiments have been performed in addition to the ice nucleation studies. One of these experiments (IN11_2) is discussed in the present paper in terms of the dependence of the linear depolarization ratio on the microphysical details of plate-type ice

crystals. Before the experimental results are discussed in section 4, the following two subsections describe briefly two basic AIDA instruments that are employed routinely in those ice cloud experiments, namely the optical particle counter WELAS and the laser light scattering and depolarization instrument SIMONE.

3.1. WELAS

A commercial optical particle counter WELAS (WhitE Light Aerosol Spectrometer, [28]) is mounted below the chamber inside the thermostated housing (see figure 5). The OPC is used to measure number density and size distribution of liquid particles in the size range from 0.5 to 48 μm. In contrast to spherical particles, WELAS cannot size ice crystals accurately because the apparent size of an ice crystal depends on the shape and the accidental random orientation of the crystals in the detection volume. However, WELAS can well distinguish between larger ice crystals and smaller droplets.

3.2. Depolarization Instrument

The in situ laser light scattering and depolarization instrument SIMONE (the Scattering Intensity Measurements for the Optical detectioN of icE instrument in figure 5) is described in detail elsewhere [29]. Here, we give only a rough description of the set up and the measured quantities. SIMONE uses a continuous wave semiconductor laser (λ= 488 nm, 10 mW) to generate a polarized and collimated light beam which is directed horizontally along the diameter of the AIDA chamber. The linear polarization

state of the incident light beam can be adjusted by using a liquid crystal polarization rotator in front of the laser head. It is usually aligned either parallel or perpendicular to the scattering plane, defined by the light beam and the overlapping detection apertures of two telescopes. The telescopes probe scattered light from the chamber interior at 2° in forward direction and at 178° in backward direction. The intersection between the laser beam and the telescope apertures in the center of the chamber defines the detection volume of the instrument of about 7 cm^3. While the intensity of forward scattered light is measured directly by a photomultiplier, the polarization state of the backscattered light is analyzed by using a Glan-Taylor prism prior to the detection by two photomultipliers. In this way the parallel ($I_{||}$) and perpendicular ($I_{\perp}$) intensity components with respect to the scattering plane are measured. From these experimental quantities, the averaged linear depolarization ratios $\delta_{||}$ and $\delta_{\perp}$ of the nucleated ice crystals for incident light polarized parallel or perpendicular to the scattering plane are deduced:

$$\begin{aligned} \delta_{||} &= \frac{I_{\perp} - I_{\perp}^{bs}}{I_{||} - I_{||}^{bs}} \quad \text{for parallel polarized incident light} \\ \delta_{\perp} &= \frac{I_{||} - I_{||}^{bs}}{I_{\perp} - I_{\perp}^{bs}} \quad \text{for perpendicular polarized incident light.} \end{aligned} \tag{3}$$

$I_{||}^{bs}$ and $I_{\perp}^{bs}$ are the backscattered intensities polarized parallel and perpendicular to the scattering plane. In this way, the linear depolarization ratio can be determined with an accuracy of 0.05 at a temporal resolution of 1 s. To compare with modeling results we need to express the depolarization defined in equation (3) by elements of the scattering matrix. By means of the definition of the Stokes vector, the intensities in equation (3) can be written as follows,

$$\begin{aligned} I_{||} - I_{||}^{bs} &= \frac{I_{sca} + Q_{sca}}{2} \\ I_{\perp} - I_{\perp}^{bs} &= \frac{I_{sca} - Q_{sca}}{2}, \end{aligned} \tag{4}$$

where I_{sca} and Q_{sca} are elements of the Stokes vector of the scattered light [30]. Next, I_{sca} and Q_{sca} can be obtained by applying the scattering matrix to the incident Stokes vector. The corresponding Stokes vector elements of scattered light for polarization of the incident light parallel and perpendicular to the scattering plane are $I_{sca||}, Q_{sca||}$ and $I_{sca\perp}, Q_{sca\perp}$ respectively.

$$\begin{aligned} I_{sca||} = \frac{S_{11} + S_{12}}{R^2}; \quad I_{sca\perp} = \frac{S_{11} - S_{12}}{R^2} \\ Q_{sca||} = \frac{S_{12} + S_{22}}{R^2}; \quad Q_{sca\perp} = \frac{S_{12} - S_{22}}{R^2}. \end{aligned} \tag{5}$$

The constant R is the distance from the scatterer. Note that $S_{21} = S_{12}$ for randomly oriented ice crystals. Inserting equations (4) and (5) into equation (3) gives

$$\delta_{||} = \frac{S_{11} - S_{22}}{S_{11} + 2S_{12} + S_{22}} = \frac{1 - S_{22}/S_{11}}{1 + 2S_{12}/S_{11} + S_{22}/S_{11}}$$

$$\delta_{\perp} = \frac{S_{11} - S_{12}}{S_{11} - 2S_{12} + S_{22}} = \frac{1 - S_{22}/S_{11}}{1 - 2S_{12}/S_{11} + S_{22}/S_{11}}.$$

4. Experimental and modeling results

The specific experiment discussed here was started at an initial gas temperature of 252.5 K (plate regime in [7]) at nearly ice saturated conditions (both quantities still levelled off from the previous expansion). At 2916 s experiment time, water droplets were injected into the AIDA volume by an atomizing nozzle. The water droplet injection lasted for 148 seconds indicated by the thin vertical dotted lines in figure 6. A fraction of the supercooled water droplets started to nucleate ice during the injection probably by expansion cooling resulting in a localized mixed-phase cloud. During its spreading into the AIDA volume, the mixed-phase cloud rapidly converted into a pure ice cloud by the Bergeron-Findeisen process and by partial evaporation of the droplets during their injection into the chamber which is subsaturated with respect to water, but slightly supersaturated with respect to ice. The HOLIMO detector described in this paper was used during this experiment to characterize the habit distribution of the ice particles in the simulated clouds. Hydrometeors were sucked out of the AIDA

chamber with an average velocity of 1.3 m s^{-1}. Hence a particle with a maximum diameter of 30 μm would have a Reynolds number of 3. The distance hydrometeors travel from AIDA to HOLIMO sample volume was about 1 m. Therefore, such large ice crystals have sufficient time to align preferably in horizontal orientation [31]. Figure 5 shows the setup of the AIDA chamber and the position of measurement of HOLIMO. It was placed at the bottom of the chamber with a strictly vertical sampling line in order to avoid particle loss due to sedimentation.

Figure 6 depicts p, T, s_i (the ice saturation ratio), WELAS and HOLIMO size distributions, scattering intensities and depolarization ratio data on the panels a, b, c, d, e and f respectively. WELAS indicates a maximum ice crystal number concentration around 3400 s after the start of the experiment (panel c) when HOLIMO started recording the most images of particles per second (panel d). It performed single particle detection throughout this experiment and hence a particle density of one particle per V_{obs} was recorded. The largest number of hydrometeors seen by HOLIMO between 3400 and 4000 s also indicates a maximum in number of ice crystals. WELAS shows another maximum on panel c at the time of supercooled water droplet injection. Temperature and s_i values are given with an accuracy of $\pm$0.3 K and $\pm$5% accordingly. The HOLIMO sizes are associated with an error of $\pm$ 15% (see subsection "theory of operation").

Panel a shows the evolution of the mean gas temperature inside AIDA during the

expansion cooling experiment. While the wall temperature of the vessel stayed rather constant throughout the whole experiment, the droplet injection (region between vertical lines) leads to an increase of the mean gas temperature. After this event one can observe a constant decrease of the gas temperature until the point where the expansion cooling leveled off due to the heat flux from the warmer chamber walls.

Panel *b* shows the ice saturation ratio with respect to the interstitial and total (interstitial and particulate) water contents inside AIDA. The injection of supercooled water droplets is clearly visible in an increase of the particulate water content. Meanwhile, the emerging ice cloud reduced the interstitial water vapor content and confined the saturation ratio to ice saturated conditions after a short period of enhanced fluctuations during droplet injection. The interstitial phase remained close to a saturation ratio of 1 after the injection.

Panel *c* is obtained from the WELAS optical particle counter and reveals 2 modes of particle growth. The first and bigger mode with respect to the optical particle diameter emerged during the time of injection. The second mode grew directly after the first mode vanished. It is very likely that these two modes reflect the spray characteristics of the atomizing nozzle. As already mentioned, the droplets were probably freezing due to the expansion of the spray. Some of the ice crystals may have grown fast to thick plates at relatively high supersaturation with respect to ice and close to water saturation within undiluted sections of the cloud of the spray. They may have sedimented while others were transported into regions with less or no super-

cooled droplets. Those crystals may have grown slowly, due to a small but existing supersaturation with respect to ice, from very small crystals in the beginning to very large thin plates that aggregated at the very end of the experiment. An overview of ice crystal habits taken with HOLIMO supports this interpretation of the evolution of the measured size distribution (figure 7). Note that WELAS underestimates sizes of ice crystals in general. The ice crystal orientation becomes important especially for thin ice crystals with large aspect ratios χ of maximum length versus thickness. Those ice crystals lead to a wide spread of measured optical particle diameter shown during period III of this panel.

The maximum particle diameter deduced from HOLIMO images is shown on panel *d*. 81% of the particles found within period I from 3000 to 3400s were identified. Table 1 shows that they split into 5% thin, 74% thick plates and 22% aggregates of thick plates. Most of the particles emerging from period II from 3400 to 4000s were either too small for HOLIMO to resolve their habits or they were out of focus. Therefore, the automated routine only identified 36% of the particles. Among these particles 68% thin and 28% thick plates have been found (see table 1). In period III from 4000 to 4600s, 78% of the observed particles were identified. 93% of them were thin plates and 7% aggregates of them (see table 1). Larger particles were seen during period I than during period II because of ice crystal sedimentation (average maximum particle diameter of 17 μm compared to 13 μm). The volume of thick and thin ice crystal plates with a maximum particle diameter of 20 μm is $2.9{\cdot}10^{-9}$ cm^{-3}

and $1.9{\cdot}10^{-9}$ cm^{-3} respectively [32]. Therefore, thick hexagonal ice crystal plates and aggregates of thick plates are heavier and sediment faster than equally sized thin hexagonal ice crystal plates and their aggregates. The particles detected in period I were smaller than the ones observed during period III (average maximum particle diameter 28 μm) since thick hexagonal plates and their aggregates have a larger fall velocity than thin hexagonal plates. The latter ones can thus grow to larger sizes and remain airborne over longer times.

This habit distribution leads to an interesting result substantiated in panel e and f. They show the scattered intensity (total, forward and backward) and the linear depolarization ratios $\delta_{||}$ and $\delta_{\perp}$. The depolarization ratio for parallel incident laser polarization $\delta_{||}$ reveals very low values between 0.11 for the thick plates shortly after the droplet injection and 0.04 for the large thin plates towards the end of the experiment. Between 3700s and 4000s the incident laser polarization was changed to be directed perpendicular to the scattering plane. The corresponding depolarization ratio $\delta_{\perp}$ is offset by about 0.04 with respect to $\delta_{||}$. Even more striking than these low values is the trend of both quantities. $\delta_{||}$ starts off in the beginning of period I around 0.1 indicating first thick plates and aggregates conglomerated of them. The depolarization ratio then decreased after thick plates and their aggregates started to sediment (first mode of the WELAS data). This trend continues because the fraction of thick plates decreased further while the fraction of thin plates increased. Additionally, during period III, the thin plates were growing larger and aggregated.

To understand the behavior of the linear depolarization ratio by comparison with the results from ray tracing calculations described below in this section, it is important to know the aspect ratio χ of the plates. Pictures of thin plates under a grazing angle and thick plates were analyzed in order to determine χ. Figure 8 shows some χ values assigned to thick and thin plates for a few example pictures. It is better to use thin plates under a grazing angle to estimate their thickness because the effect of edge blurring of both the forward and rearward faces adds up if only one of the two opposite thin prism facets of the plate is seen. It was found that χ for thick plates ranged from 1.1 to 4.1 with a standard deviation of 0.9 and for thin plates from 9 to 65 with a standard deviation of 14.7. The linear depolarization ratios in figure 6, panel *f* are also shown with respect to χ inferred from HOLIMO ice crystal habit measurements. The values shown along the x axis were obtained from a second order polynomial fit for region I and III. χ remained around 2 without any significant trend in region II due to the small sizes of the ice crystals.

In order to assist the interpretation of the depolarization measurements, calculations for randomly oriented hexagonal prisms were carried out using a geometric optics ray tracing program [33]. In ice crystal prisms, internally reflected and refracted ray paths will be chiefly responsible for backscattering. These processes result in the reorientation of the incident polarization vector at every interface, leading to depolarization when the backscattered ray is transposed into the initial plane of polarization [34]. Figure 9 shows the calculated $\delta_{||}$ and $\delta_{\perp}$ at 178° scattering angle for a

range $1/3 < \chi < 288$. In agreement with the measurements, $\delta_{||}$ and $\delta_{\perp}$ decrease with increasing χ, and $\delta_{\perp}$ is larger than $\delta_{||}$, although the modeled depolarization values $\delta_{||}$ are higher by about 0.1. This discrepancy might partly be due to the low thickness of the investigated ice crystals, for which geometric optics is at the margin of its applicability. Notable in figure 9 are three plateaus for $\chi < 1.5$, $2 < \chi < 18$ and $18 < \chi < 80$. These plateaus are caused by contributions from specific ray paths. For near backscattering depolarization to occur, ray interaction with basal facets as well as prism facets (with the corresponding prism angles between them) are necessary. Therefore, depolarization is strongest in compact prisms ($1/3 < \chi < 1$), see e.g. ray path in figure 10a. For $1.5 < \chi < 100$ the largest contribution to the intensity of the light scattered at 178° is due to rays entering and leaving through the same basal facet after being internally reflected at the opposite basal facet and one prism facet (figure 10b). These rays cause most of the linear depolarization for $\chi > 18$. For $2 < \chi < 18$ the largest contribution to depolarization stems from the slightly stronger depolarizing ray path shown in figure 10c. For $\chi > 100$ depolarization decreases sharply due to the increasing number of rays which are reflected and refracted at basal facets only.

5. Conclusion

The digital in-line holographic microscopes HOLIMO, developed at ETH Zurich, can resolve and classify small hydrometeors down to a size of 4 μm. The algorithm for particle recognition proved to work reliably. Nevertheless, the number of particles

that can be attributed correctly to their classes depends on several things. The most important one is to have a good in-focus image of the particle. Otherwise, the habit classification scheme ends up attributing the actual hydrometeor to the wrong particle habit class. Therefore, control of the outcome by eye becomes necessary.

HOLIMO has been successfully tested in a measurement campaign at the Institute for Meteorology and Climate Science at the Forschungszentrum Karlsruhe in Germany. This study concentrates on data sets about mixed phase clouds initiated from supercooled water droplets. Very low values of the linear depolarization ratio below 0.12 have been found during such a cloud evolution event. The decreasing trend of the parallel channel of the linear depolarization ratio from 0.1 to 0.04 is accompanied by the increasing trend of χ from 2 to 20. These low and experimentally found values of the linear depolarization ratio match with the deduced aspect ratio χ of the ice crystals obtained from their habits detected by HOLIMO. To the best of our knowledge such low linear depolarization ratio values for randomly oriented thin ice crystal plates have never been reported to date. The results are supported by geometric optics ray tracing calculations for thin plates. Plates with the described properties show very low linear depolarization ratio values that can not be distinguished from those of water droplets. This implies the possibility that small values of depolarization not only stem from liquid clouds embedded in ([35]) but also from regions of randomly oriented thin plates inside of a cirrus cloud.

Onward work with HOLIMO on different ice crystal habits and their linear depo-

larization ratios are planned. Further studies on the surface structure of ice crystals and ice particle fall speed measurements are possible, because this instrument has a high time and spatial resolution and is portable. Hence, we intend to use it at the high alpine research station on the Jungfraujoch in the Bernese Alps in Switzerland and in airborne in-cloud measurements. Improvement of HOLIMO regarding the resolution of the reconstructions can be done in the future. The results from the experiments described in this paper revealed that it is more important to have a large numerical aperture instead of having a large geometrical magnification. Therefore, the most promising step towards increased resolution will be to shorten the distance from the point source to the camera in order to decrease the error made by edge smearing. Here also a trade off must be made because increasing the numerical aperture like this suddenly leads to a decrease of geometrical magnification and smaller objects can no longer be resolved when the fringe separation is too small for the camera to be recorded.

Acknowledgments

This work was supported by the ETH Zurich research grant TH-39/05-1 '*Development of an in-line Holographic Microscope for Ice Crystals*'. The authors are grateful to R. Schön from the Institute of Meteorology and Climate Research at the Forschungszentrum Karlsruhe, Germany for the help during the IN11 campaign in November 2007. Part of the work was supported by the Helmholtz Association within the framwork

of the Virtual Institute "Aerosol Cloud Interactions"

References

1. V. J. Schaefer, *The production of ice crystals in a cloud of supercooled water droplets,* Science **104**, 457–459 (1946).

2. G. Vali, *Ice nucleation-a review,* Nucleation and Atmospheric Aerosols p. 18 (1996).

3. U. Lohmann and J. Feichter, *Global indirect aerosol effects: a review,* Atmos. Chem. Phys. **5**, 715–737 (2005).

4. A. Korolev and G. A. Isaac, *Relative Humidity in Liquid, Mixed-Phase, and Ice Clouds,* J. Atmos. Sci. **63**, 2865–2880 (2006).

5. M. Wendisch, P. Pilewskie, J. Pommier, S. Howard, P. Yang, A. J. Heymsfield, C. G. Schmitt, D. Baumgardner and B. Mayer, *Impact of cirrus crystal shape on solar spectral irradiance: A case study for subtropical cirrus,* J. Geophys. Res. **110**, 1–17 (2005).

6. W. Cantrell and A. Heymsfield, *Production of ice in tropospheric clouds - a review,* Bull. Am. Meteorol. Soc. **86**, 795–807 (2005).

7. K. G. Libbrecht, *The physics of snow crystals,* Rep. Prog. Phys. **68**, 855–895 (2005).

8. P. Yang, H. Wei, H. L. Huang, B. A. Baum, Y. X. Hu, G. W. Kattawar, M. I. Mishchenko and Q. Fu, *Scattering and absorption property database for nonspher-*

ical ice particles in the near- through far-infrared spectral region, Appl. Opt. **44**, 5512–5523 (2005).

9. H. J. Kreuzer, M. J. Jericho, I. A. Meinertzhagen, and W. B. Xu, *Digital in-line holography with photons and electrons,* J. Phys.: Condens. Matter **13**, 10729–10741 (2001).

10. J. D. Trolinger, *Particle field holography,* Opt. Eng. **14**, 383–392 (1975).

11. J. Sheng, E. Malkiel, and J. Katz, *Digital holographic microscope for measuring three-dimensional particle distributions and motions,* Appl. Opt. **45**, 3893–3901 (2006).

12. P. R. A. Brown, *Use of holography for airborne cloud physics measurements,* J. Atmos. Oceanic Technol. **6**, 293–306 (1989). USA.

13. J. P. Fugal, R. A. Shaw, E. W. Saw, and A. V. Sergeyev, *Airborne digital holographic system for cloud particle measurements,* Appl. Opt. **43**, 5987–5995 (2004).

14. H. J. Vossing, S. Borrmann, and R. Jaenicke, *In-line holography of cloud volumes applied to the measurement of raindrops and snowflakes,* Atmos. Res. **49**, 199–212 (1998).

15. S. M. F. Raupach, H. J. Vossing, J. Curtius, and S. Borrmann, *Digital crossed-beam holography for in situ imaging of atmospheric ice particles,* J. Opt. A: Pure Appl. Opt. **8**, 796–806 (2006).

16. S. K. Jericho, J. Garcia-Sucerquia, W. B. Xu, M. H. Jericho, and H. J. Kreuzer,

Submersible digital in-line holographic microscope, Rev. Sci. Instr. **77**, 10 (2006).

17. J. W. Goodman, *Introduction to Fourier Optics,* Roberts & Company **3rd edition**, (2005).

18. C. S. Vikram and M. L. Billet, *In-line Fraunhofer holography at a few far fields,* Appl. Opt. **23**, 3091–3094 (1984).

19. J. Garcia-Sucerquia, W. B. Xu, S. K. Jericho, P. Klages, M. H. Jericho, and H. J. Kreuzer, *Digital in-line holographic microscopy,* Appl. Opt. **45**, 836–850 (2006).

20. C. S. Vikram and M. L. Billet, *Some salient features of in-line Fraunhofer holography with divergent beams,* Optik **78**, 80–83 (1988).

21. D. M. Robinson, *A calculation of edge smear in far-field holography using a short-cut edge trace technique,* Appl. Opt. **9**, 496–497 (1970). USA.

22. S. L. Cartwright, P. Dunn, and B. J. Thompson, *Noise and resolution in far-field holography,* J. Opt. Soc. Am. **70**, 1631–1631 (1980).

23. B. J. Thompson, *Holographic particle sizing techniques,* J. Phys. E (Sci. Instr.) **7**, 781–788 (1974). UK.

24. H. Koehler, *On Abbe's theory of image formation in the microscope,* Optica Acta **28**, 1691–1701 (1981).

25. C. Magono and C. Lee, *Meteorological classification of natural snow crystals,* J. Fac. Sci. **2**, 321–335 (1966). Hokkaido University Series VII.

26. A. Korolev, G. A. Isaac, and J. Hallett, *Ice particle habits in stratiform clouds,*

Q. J. R. Meteorol. Soc. **126**, 2873–2902 (2000). 46 Part A.

27. O. Möhler, S. Büttner, C. Linke, M. Schnaiter, H. Saathoff, O. Stetzer, R. Wagner, M. Krämer, A. Mangold, V. Ebert, and U. Schurath, *Effect of sulfuric acid coating on heterogeneous ice nucleation by soot aerosol particles,* J. Geophys. Res. **110**, D11210 (2005).

28. S. Benz, K. Megahed, O. Möhler, H. Saathoff, R. Wagner, and U. Schurath, *T-dependent rate measurements of homogeneous ice nucleation in cloud droplets using a large atmospheric simulation chamber,* J. Photochem. Photobiol., A **176**, 208–217 (2005).

29. M. Schnaiter, S. Benz, V. Ebert, T. Leisner, O. Möhler, R. W. Saunders, and R. Wagner, *Influence of particle size and shape on the backscattering linear depolarization ratio of small ice crystals,* J. Atmos. Sci. (2009). To be submitted.

30. H. van de Hulst, *Light scattering by small particles* (Dover Publications, Inc, New York, 1981).

31. J. Hallett, *Faceted snow crystals,* J. Opt. Soc. Am. A **4**, 581–588 (1987).

32. H. R. Puppacher and J. D. Klett, *Microphysics of Clouds and Precipitation* (Kluwer Academic Publishers, 1997).

33. A. Macke, J. Mueller, and E. Raschke, *Single scattering properties of atmospheric ice crystals,* J. Atmos. Sci. **53**, 2813–25 (1996).

34. K. Sassen, *Light scattering by nonspherical particles* (New York: Academic Press,

1999).

35. K. Sassen and S. Benson, *A Midlatitude Cirrus Cloud Climatology from the Facility for Atmospheric Remote Sensing. Part II: Microphysical Properties Derived from Lidar Depolarization,* J. Atmos. Sci. **58**, 2103–2112 (2001).

Appendix: List of symbols

$2a$	maximum particle diameter
c	particle concentration
d	resolution limit
d_{equiv}	sphere equivalent diameter
D_{max}	maximum diameter parallel to streamlines of sample flow
D_w	maximum diameter perpendicular to streamlines of sample flow
m	number of airy rings
m_0	wavelength dependent magnification
m_1	geometric magnification
M	overall magnification
N	number of far field distances
N_{pix}	amount of pixels
V_{obs}	observing volume of HOLIMO
α	D_w/D_{max} if $D_w < D_{max}$ or D_{max}/D_w if $D_w > D_{max}$
δ	linear depolarization ratio
Δ_l	reconstruction plane separation
Δ_x, Δ_y	pixel size on the camera
Δ_X, Δ_Y	pixel size on the reconstruction plane
λ	wavelength of the light source
λ_{eff}	wavelength with respect to the medium
χ	aspect ratio of length over thickness

Table 1. Frequency of occurrence of ice crystal habits in 3 different periods of experiment IN11_2.

period:	I	II	III
identified particles [%]	81	36	78
thin plates [%]	5	68	93
thick plates [%]	74	28	0
aggregates of thin plates [%]	0	2	7
aggregates of thick plates [%]	22	2	0

List of Figures

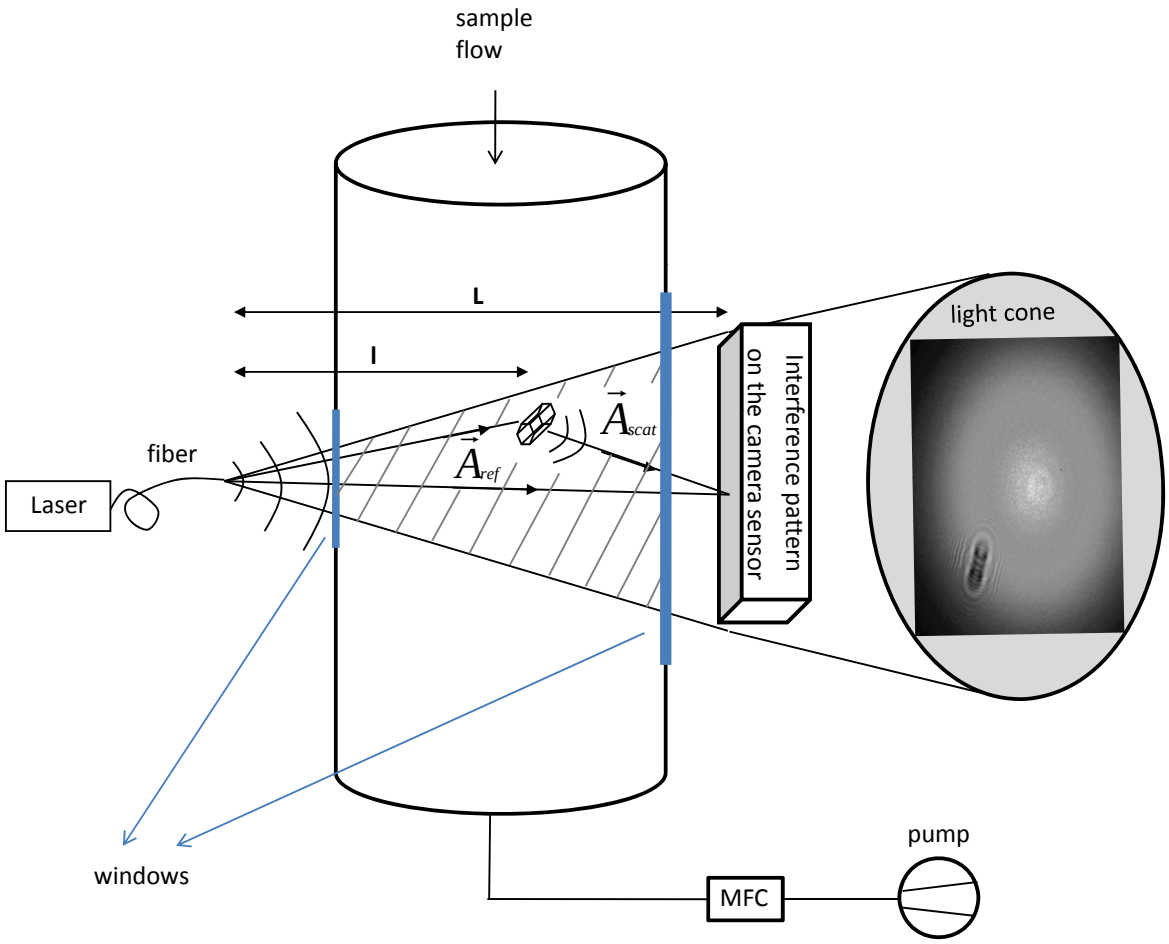

Fig. 1. Sketch of the working principle of HOLIMO. It shows the recording setup. The reconstruction is done numerically. In the main the setup consists of a laser point source of light and a CCD camera that records the interference pattern of the reference wave with the scattered wave amplitude from an object inside the sample flow tube that is sealed off from the camera and the laser by 2 windows. The observing volume is indicated with the hatched area. A possible interference pattern on the camera sensor inside the light cone is shown on the right hand side of the sketch. Objects are sucked through the sample flow tube with the help of a vacuum pump. The mass flow controller (MFC) controls the flow.

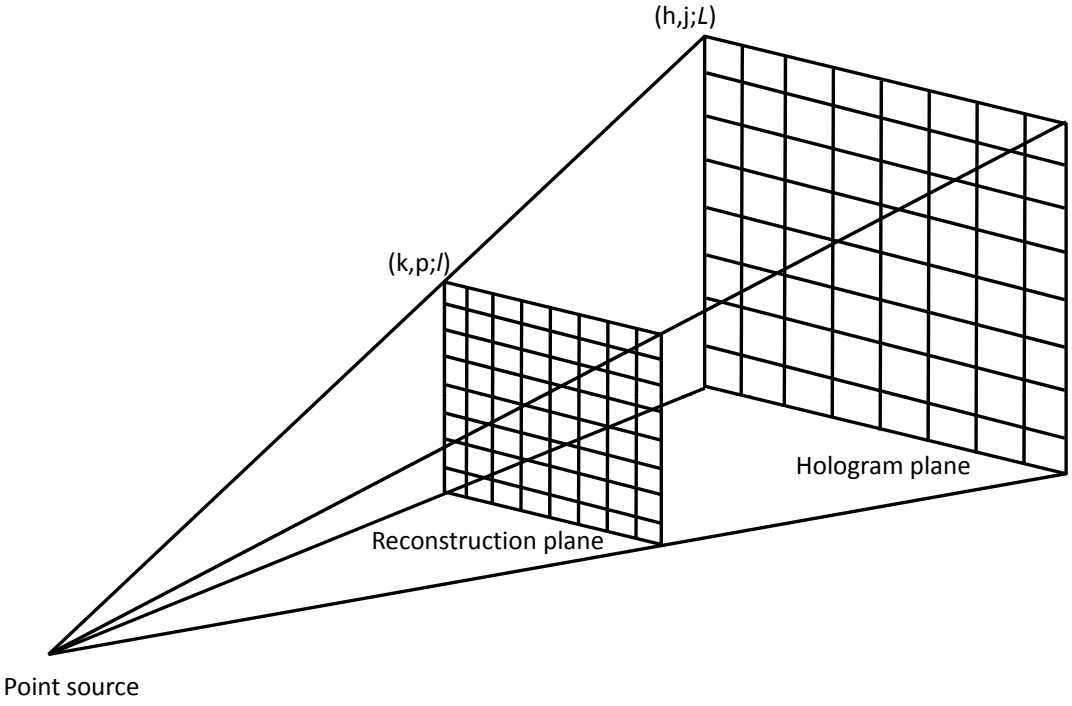

Fig. 2. Illustration of a reconstruction plane inside V_{obs} of HOLIMO. Every pixel (k, p) of this reconstruction is calculated at the position l adding up all contributions of the pixels of the camera at the points (h, j) at the position L.

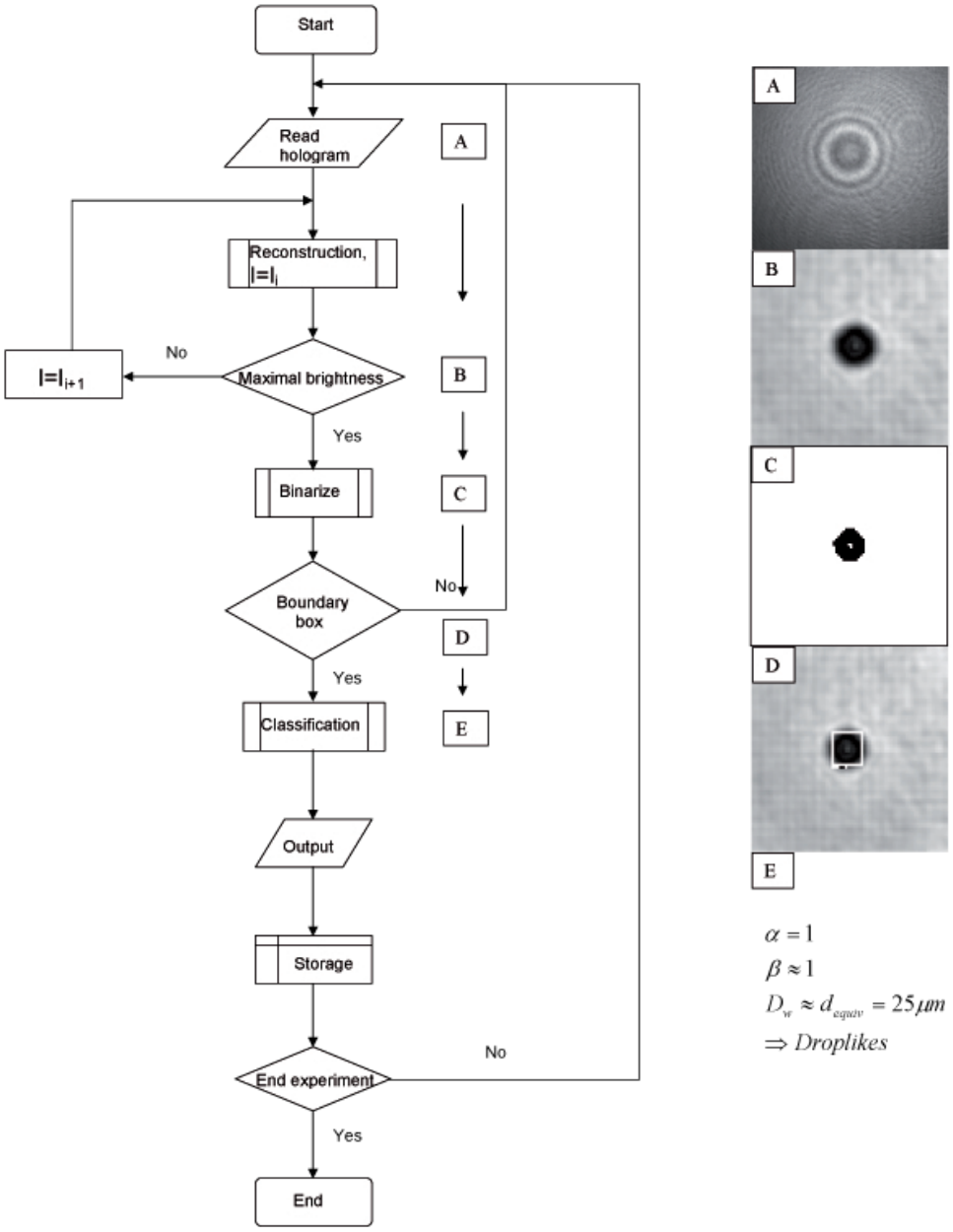

Fig. 3. Flow chart of the data processing of HOLIMO (left panel). First the hologram will be read in and a predefined routine reconstruction produces the image of maximal brightness at a distance l_j. The image needs to be binarized in order to define a boundary box. This makes it possible to classify the objects in a predefined routine and store the important findings. Every hologram is treated in the same manner before the data processing is ended. An example of this process is shown on the right hand side. Frame A shows the hologram, frame B its reconstruction and frame C its binary representation. Frame D includes the boundary box with the binary size label d_{equiv} underneath the box and frame E attributes the object to the class droplikes.

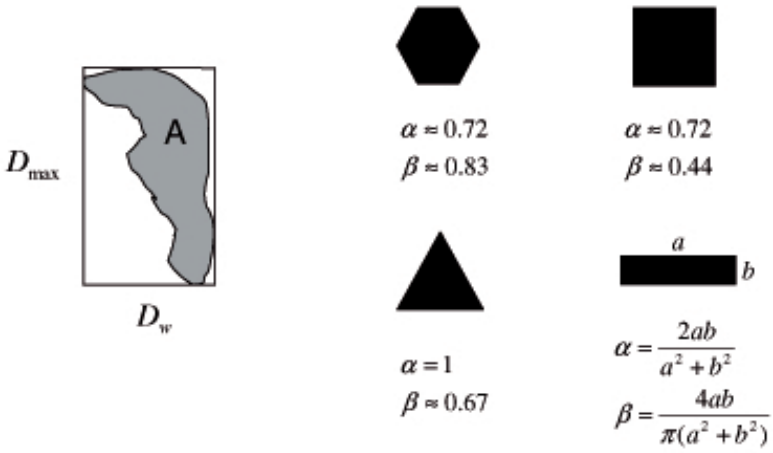

Fig. 4. Classification scheme for HOLIMO images of hydrometeors inside a sample flow. The measurable parameters D_w (parallel to the streamlines), D_{max} (horizontal to the streamlines), A and the circumference are used for image habit recognition. Examples of the aspect ratio $\alpha = D_w D_{max}^{-1}$ and the roundness $\beta = 4A(\pi D_{max}^2)^{-1}$ are given for 4 simple shapes.

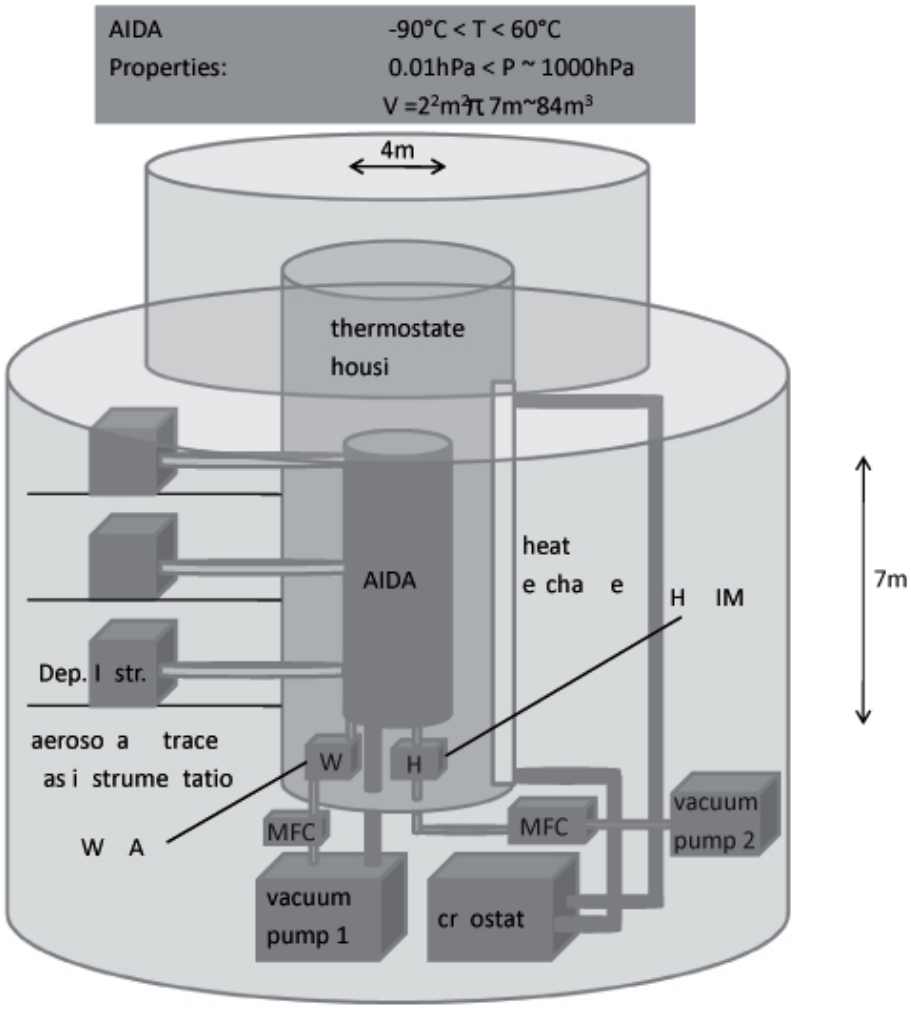

Fig. 5. Sketch of the AIDA facility. AIDA itself is the inner most cylinder. It has a diameter of 4 m and is 7 m high. This corresponds to a volume of approximately 84 m^3. It is surrounded by a thermal housing and aerosol and trace gas instruments. The wall temperature of AIDA is adjusted via heat exchange controlled by a cryostat in the basement. The temperature can be set between $-90°$ C and $+60°$ C. The inner temperature is controlled via adiabatic expansion with a vacuum system in the basement. The pressure can be set between 0.01 hPa and 1000 hPa. The vacuum system is also used for various sampling streams which are drawn off from the bottom of AIDA and controlled with a MFC. The point where HOLIMO was inserted into the measuring flow is indicated.

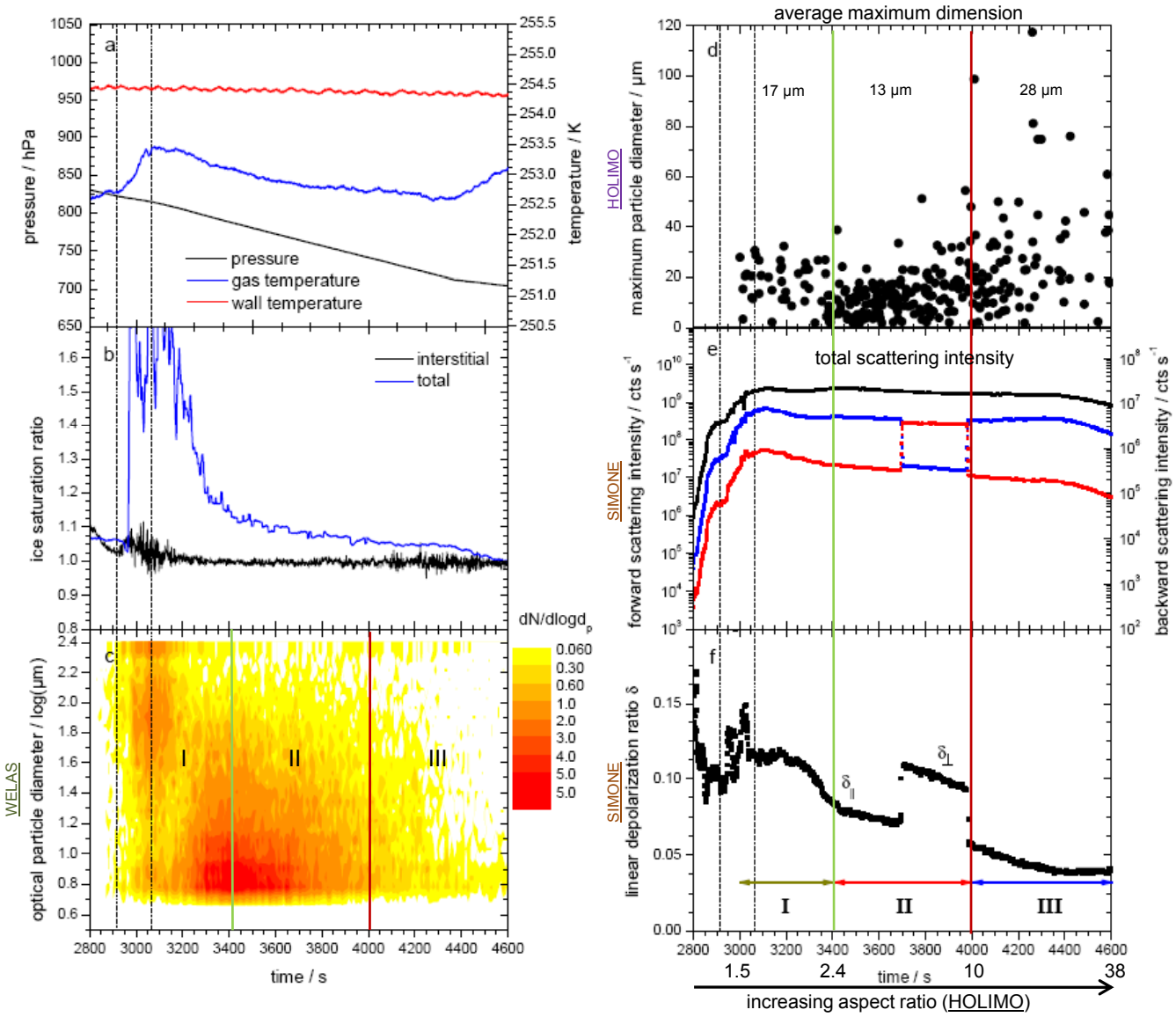

Fig. 6. Temporal evolution of the AIDA mixed phase cloud experiment 2. Panel *a*: wall temperature of plus gas temperature and pressure inside AIDA. Panel *b*: ice saturation ratio of the total and interstitial water content s_i inside AIDA. Panel *c* and *d*: WELAS and HOLIMO size distribution respectively. Data are subsequently divided into 3 regions (I, II and III), based on different levels (high, medium, low) of the linear depolarization ratio. Panel *e*: backward scattered signal of the perpendicular and the parallel channel in blue and red with respect to the total forward scattered signal in black. Panel *f*: linear depolarization ratio of the 2 backward channels with respect to time and χ in region I and III. The vertical lines at the beginning of the experiment throughout all panels indicate the time of droplet injection.

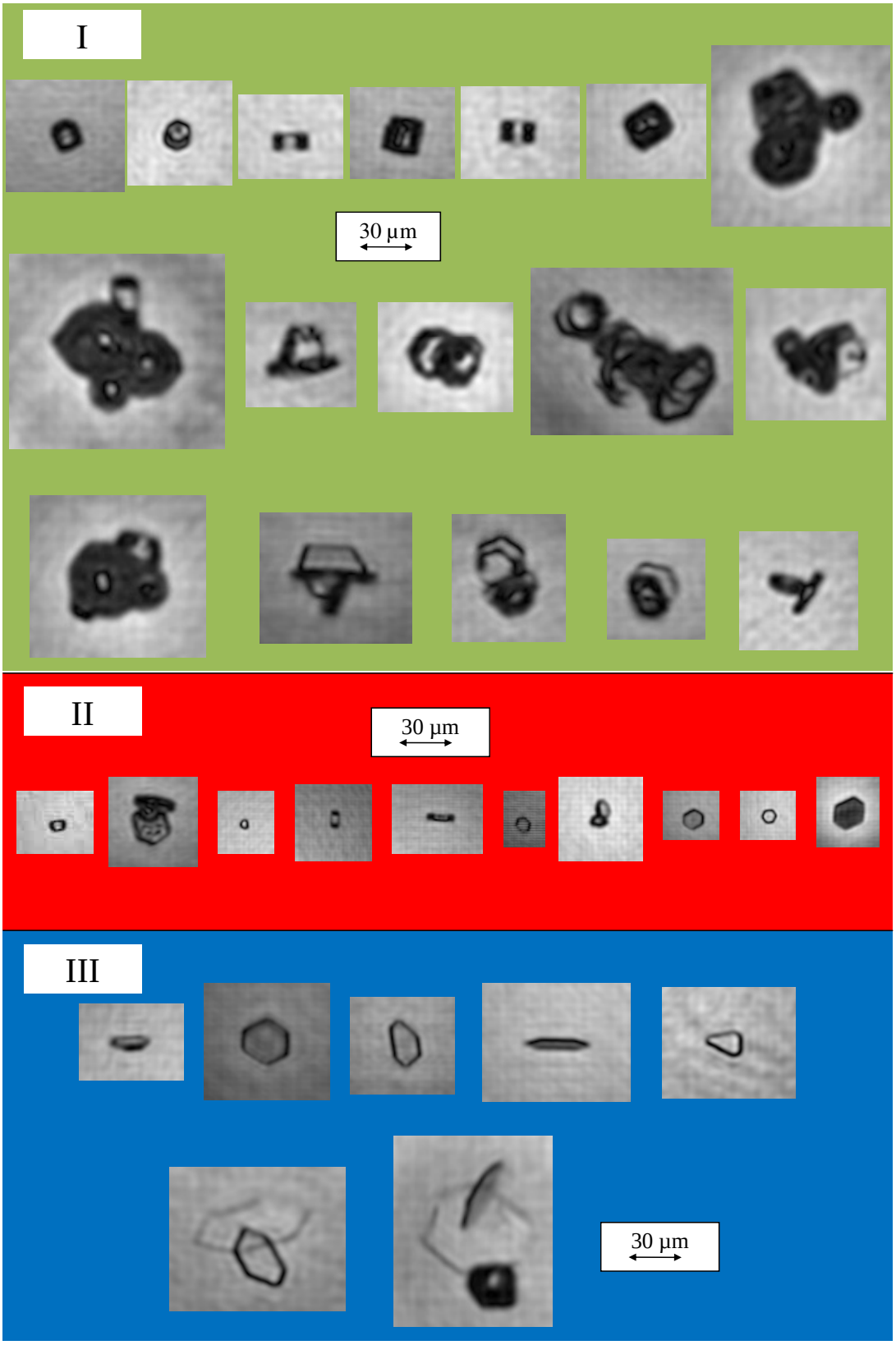

Fig. 7. Ice crystal habits of experiment 2 during three different time slots showing three different phases of habits and frequency of occurrences.

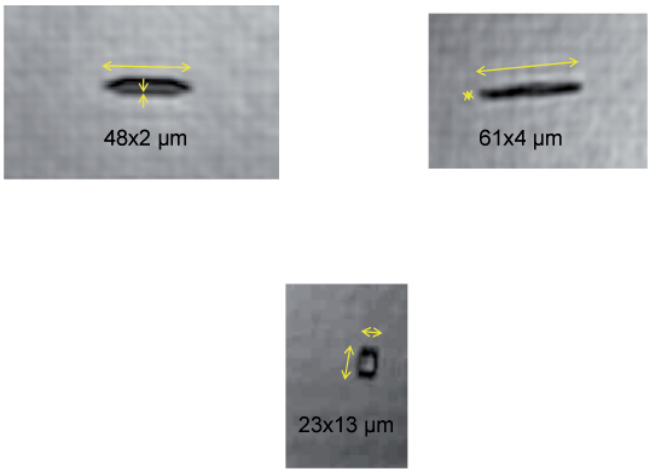

Fig. 8. Example pictures of aspect ratios χ = maximum length/thickness for thin and thick plates. $\chi = 24$ for the thin plate seen under grazing incident angle (upper left panel). $\chi = 15$ for the thin plate in the upper right panel. Here the contribution of edge blurring is bigger than for the previous example because both the forward and rearward faces add up. The thick plate in the lower panel has $\chi = 2$.

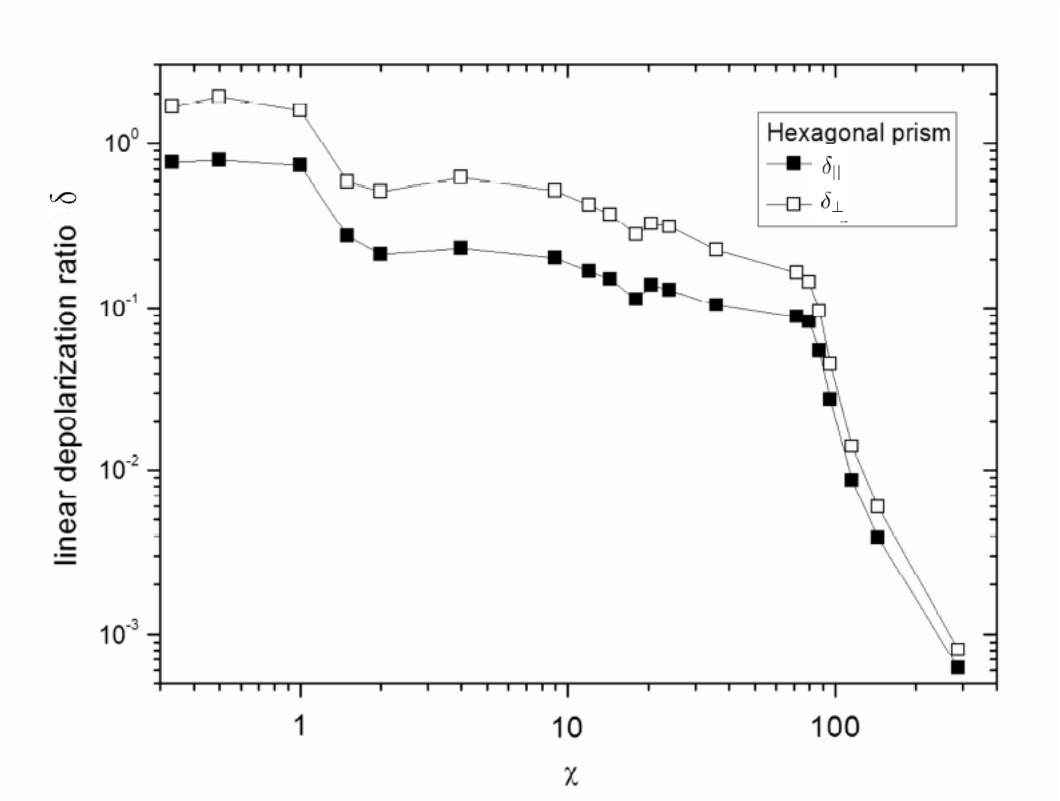

Fig. 9. Linear depolarization ratios vs. χ of randomly oriented hexagonal prisms calculated using geometric optics.

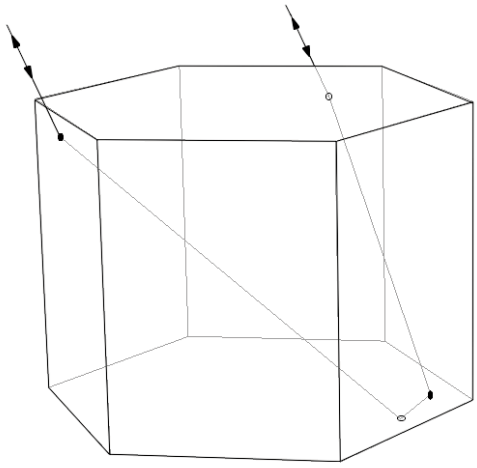

(a)